Andreev reflections and superconducting Proximity effect in lateral hBN/graphene/$NbSe_2$ quantum Hall devices

Master thesis - Clevin Handschin

June 26, 2013

Supervisor at Columbia University: Dmitri K. Efetov and Prof. Philip Kim

Supervisor at University of Basel: Prof. Christian Schönenberger

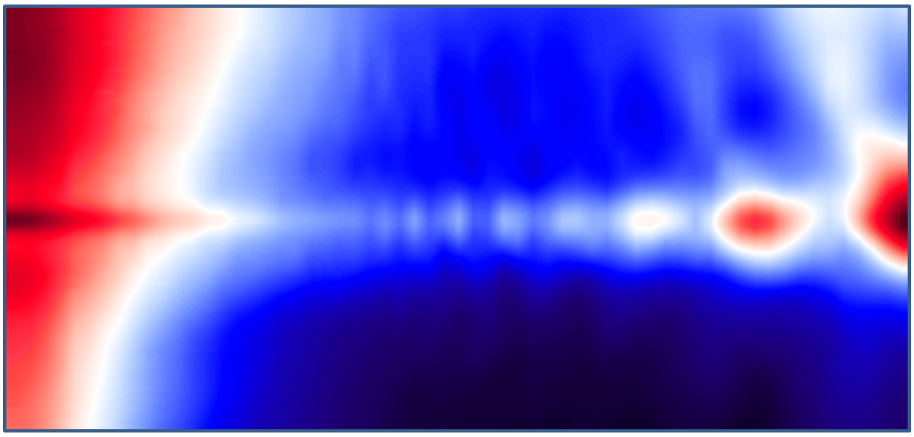

COLUMBIA UNIVERSITY
IN THE CITY OF NEW YORK

UNI
BASEL

Abstract

For the first time a layered superconductor ($NbSe_2$) was coupled to a high quality bilayer graphene (BLG) Hall bar (μ ~110'000 $cm^2V^{-1}s^{-1}$, onset of QHE at ~1 T) establishing a high transparency SN junction (R_{SN} ~300-1'000 Ω). A detailed characterization of the SN interface revealed a weak coupling between the BLG and the $NbSe_2$ with a maximally enhanced conductance of ~5%. Last mentioned is comparable to the best graphene/superconductor junctions available yet. Furthermore the overall SN junction resistance was found to be dominated by the Maxwell resistance accounting for inelastic quasi particle scattering. Additional dips in the differential conductance outside the superconducting energy gap could be attributed to joule heating effects of the point contact Andreev reflection spectroscopy, driving $NbSe_2$ from the superconducting to the normal conducting state. An oscillation like behavior of the zero bias conductance across the SN junction with varying magnetic field could be related to compressible and incompressible states of the QHE. Besides the expected filling factors for BLG ν=±4, ±8,... additional integer filling factors were observed. Most of the latter were found not to be related to the superconducting lead. However, for ν=-2 the question remains open if surface superconductivity is involved or not.

Contents

1 Introduction

1.1 Superconductivity

The effect of superconductivity, meaning that a certain material has *zero electrical resistance*[1], was discovered 1911 by H. Kamerlingh Onnes in Leiden by investigating the electrical properties of mercury at low temperatures. [2] The next great milestone to be discovered was *perfect diamagnetism* in 1933 by W. Meissner and R. Ochsenfeld. [3] So far the exclusion of an applied magnetic field from the superconductor was explained as a result of the zero resistance and Lenz's law. However, the exclusion of external magnetic fields[2], independent of the order of cool down and applied magnetic field, could not be explained by the familiar laws of electromagnetism. Consequently this effect is characteristic for superconductors and called the *Meissner effect.* In 1956 L. N. Cooper introduced for the first time the idea of bound electrons - so called *Cooper pairs.* [4] He showed that a small attraction between the electrons in a metal can cause a paired state of electrons having a lower energy than the Fermi energy. Soon after, in 1959 J. Bardeen, L. N. Cooper and J. R. Schieffer introduced their BCS-Theory which was remarkably complete and satisfactory. [5] However, in 1986 a new class of superconductors, the high-temperature superconductors (e.g. LaBaCuO: T_c= 30 K, BaYCuO: T_c= 90 K or $HgBa_2Ca_2Cu_3O_x$: 135 K - record under ambient pressure so far), was found by Bednorz and Müller. [6] Those superconductors obey the same general phenomenology as the classic superconductors, but the basic microscopic mechanism remains unsolved so far. The superconductors with a $T_c > 77$ K became of special interest for commercial applications, e.g. MRI in health care, since they can be cooled with liquid nitrogen which is much cheaper than liquid helium.

1.2 2-dimensional electron gases

A 2-dimensional electron gas (2DEG) is a gas of electrons which can freely move in two directions, but is confined in the third one. A great deal of interest is given to 2DEG[3] latest since the quantum Hall effect was discovered by K. Klitzing in 1980. [7] Besides the QHE there are several other physical effects and applications (e.g. MOSFET transistors) which depend on a 2DEG. There are several ways how 2DEG can be realized. For a long time the most common types of 2DEG were semiconductor hetero-structures, such as, e.g., GaAs/AlGaAs. However, the use of semiconductor hetero-structures leads to the formation of a Schottky barrier with the metal leads, which makes it difficult to establish transparent contacts, especially for superconductors. For a long time, strict 2D crystals such as graphene, a single layer of graphite, were presumed to be thermodynamically unstable. [8, 9] However, in 2004 this theory was proved to be wrong by the experimental discovery of free standing graphene by Novoselov *et al.* [10] The great interest and success of graphene as a 2DEG compared to other 2D systems cannot only be attributed to its simple fabrication using micro mechanical exfoliation, but much more to its many outstanding properties, such as, e.g., the linear energy dispersion relation (massless charge carriers) near the K-point, extremely high charge carrier mobilities and ballistic transport on submicron scale. Furthermore, graphene-metal contacts do not lead to the formation of a Schottky barrier, which greatly simplifies the establishment of transparent SN junctions.

[1]In principle it is only possible to give an upper limit of the resistance since it is experimentally impossible to measure zero resistance. However, a decrease in resistance by 14 magnitudes or more has been proven. [1]

[2]The magnetic field does penetrate into the superconductor for a finite distance λ which is typically in the range of around 500 $\AA$.

[3]Or 2D systems in general, including electron and hole gases.

1.3 Dielectric substrates for high mobility graphene

In the beginning graphene was mostly isolated on SiO_2 due to the simple ability to identify a SLG with an optical microscope. However, SiO_2 was found not to be the ideal support for graphene because of its high surface roughness and its varying electrical environment caused by trapped ions in its oxide layer. [11, 12] Especially the latter mentioned property of SiO_2 causes the graphene to break up into electron and hole doped regions, so called puddles, making the Dirac point physics inaccessible. [13] Hexagonal boron nitride (hBN) with its similar crystal structure to graphene[4] was found to be ideal to improve the quality of the graphene, since it has a much flatter surface and a very homogenous surface potential compared to SiO_2. [14, 15, 16] So far, graphene on hBN exhibit the highest mobilities reported on any substrate. [17]

1.4 Co-existence of superconductivity and the quantum Hall effect

2DEG under the influence of an applied magnetic field and superconductors share many interesting properties as e.g. dissipationless current flow[5]. Studying the coupling between these two systems is not only interesting on a fundamental level, but might as well have practical application in the field of topological quantum computation. [18] The combination of superconductivity and the quantum Hall effect (QHE) attracts a great deal of interest due to the many prediction related to this kind of system such as the appearance of additional edge-states in the integer QHE or the observation of Majorana fermions in the fractional QHE. [19, 20, 21] However, to experimentally achieve the co-existence of both effects proved itself as challenging, since the onset of the QHE has to be lower than the critical magnetic field of the superconductor. In order to do so, high quality 2D systems with a low onset of the QHE and a superconductor with a reasonably high critical magnetic field has to be chosen. The recent development of high quality graphene on hBN (onset of the QHE as low as $\sim$1 T) and the high compatibility with various superconductors, opened the possibility to actually test these predictions.

[4]hBN has the same, hexagonal crystal structure and a lattice constant which deviates only by 1.8% by the one from graphene.

[5]If the magnetic field is applied perpendicular to the 2DEG, only charge carriers moving along the sample edge contribute to the current flow which is ballistic.

2 Theory

Since this Master thesis deals with 2DEG (BLG) in the quantum Hall state and superconductors, the relevant theoretical concepts including some of the electrical properties of graphene, the integer QHE for BLG, Andreev reflection and the Proximity effect and the essential concepts of the BKT theory shall be described in the following chapter. All the explanations will be on a phenomenological level, as this will be sufficient for the understanding of the results presented.

2.1 Electrical properties of graphene

Graphene does have many different special properties, such as e.g. electronic, mechanical and optical, making it special of its kind. In the following, a short summary about the electronic properties which are crucial for the physical effects measured in this Master thesis shall be given. For more detail, the reader is referred to the author's Projectwork *Manufacturing of hBN supported high quality graphene Hall bar devices with a superconducting source (drain) made of* $NbSe_2$ chapter 1.2.1 and 1.2.2.

- **Band structure of few layer graphene:** SLG is the simplest case of all the few-layer graphene having just one[6] conduction (valence) band with a linear dispersion relation. For BLG, there exist two different conduction (valence) bands. Both of them have a parabolic shape near the K-point. Further away from the K-point the band structure becomes nearly linear. As long as the Fermi energy is not raised (for electrons) or lowered (for holes) too much, only one type of charge carriers exists in the system. For all few layer graphene with N>2, where N is the number of SLG sheets stacked on top of each other, there is always more than one conduction (valence) band accessible independent of the Fermi energy of the system. SLG and BLG both are semimetals or zero-gap semiconductors.
- **Mean free path (l_{mfp}):** Compared to most metals, the mean free path of graphene is very large. It can be as large as a couple of micrometers. [11, 22] Some reasons among other are the crystal structure of SLG, which is nearly free of defects, and the low thermal vibration of the lattice (phonons).

[6] Every conduction (valence) band which will be mentioned in this section could theoretically be seen as four separate bands by taking charge carriers of different spins and valleys (A or B sublattice) into account. However, for $B = 0\ T$ these four bands are identical in energy (degenerate) and dispersion and can be treated as one.

2.2 Quantum Hall effect and Landau quantization in BLG

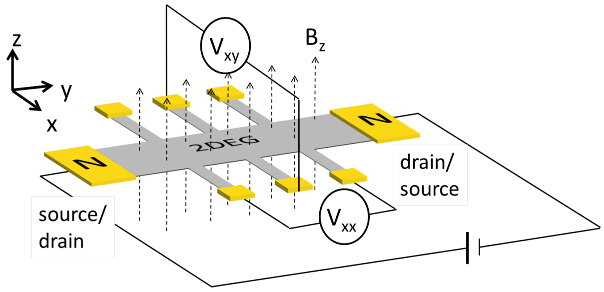

Figure 1: Sketch of a Hall bar and the setup for a 4-terminal measurement of the magneto- and Hall resistance in the QHE.

The quantum Hall effect is a quantum mechanical version of the Hall effect, which can be observed only in 2DEG which are in a strong magnetic field. In the classical Hall effect a voltage perpendicular to the current flow and the applied magnetic field can be measured according to $V_{xy} = V_H \propto IB$. The lateral, or *Hall voltage* results out of an equilibrium between the Lorenz force ($F = q\vec{v} \times \vec{B}$) and the electrostatic force ($F = eU$). By replacing the 3D Hall plate (typically a metal) by a 2DEG and by applying high magnetic fields, the QHE can be observed. In this case, the Hall voltage V_{xy} does not scale proportional with the applied magnetic field any more, but rather increases in quantized steps. A typical 4-terminal setup to measure the QHE is sketched in fig. 1. The longitudinal resistance within the Hall bar ($R_{xx} \propto V_{xx}$) is often referred to as the *magneto resistance*. The QHE is much more complicated to understand than the classical Hall effect and shall be discussed in the following. The 2DEG which is required to observe the QHE can be realized in various types of semiconducting heterostructure devices or in graphene. In the following the orientation of the 2DEG is in the xy-plane and the applied magnetic field is in the z-direction. The kinetic energy of the electrons in the system is given by $E = E_{||} + E_{\perp}$ where the second term equals zero, since no motion perpendicular to the xy-plane is possible. For $B_Z = 0$ the energy spectrum of the electrons is a continuum. By applying a magnetic field B_Z, the electrons in the system move in circular trajectories due to the Lorenz force. As a result of the periodic boundary conditions of the electron wave function, the quantized energy spectrum for a conventional 2DEG with a parabolic energy dispersion is given as

$$E_n(2DEG) = \hbar\omega_c(n + 0.5) \tag{1}$$

where $n \in \mathbb{N}_0$, $\hbar$ is Planck's constant $h/2\pi$ and $\omega_c = eB_Z/m^*$ (m^* is the effective mass of the charge carriers) is the cyclotron frequency.

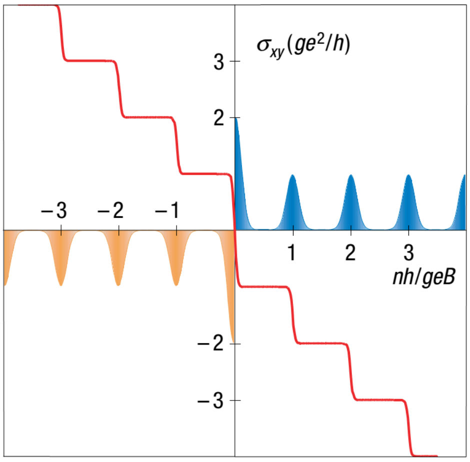

Figure 2: In BLG, the plateaus of the Hall conductivity σ_{xy} appear in quantized values of $(ge^2/h)N$, where N is a integer, e^2/h is the conductance quantum and g is the system degeneracy. The Landau levels are given as a function of the carrier concentration n, where geB/nh is the density of states. Blue and orange indicates the electron and hole doped region respectively. Figure from K.S. Novoselov et *al.* [23]

The energy dispersion of BLG differs from a parabolic 2DEG and is given by

$$E_n(BLG) = sgn(n)\hbar\omega_c\sqrt{|n|(|n|-1)} \tag{2}$$

where $n = \pm 1$, ± 2,... [24] In contrast to a conventional 2DEG, the lowest LL is at zero energy. The first LL is consequently half filled with electrons and half filled with holes as shown in fig.2. The energy levels in BLG do not scale with n (equidistant) as in parabolic 2DEG, but rather with $\sqrt{|n|(|n|-1)}$. So far, the Zeeman splitting (spin splitting) was not taken into account. It will split each LL into two separate LL with an energy difference of $E_Z = g^*\mu_B B$ where g^* is the effective Landé factor and μ_B is the Bohr magneton. Even for large magnetic fields E_Z/E_F is rather small (in the order of 1%). [25] The Hall resistance for a parabolic 2DEG is given as

$$\rho_H(2DEG) = \frac{h}{gNe^2} \tag{3}$$

where gN is the *filling factor*. The degeneracy of the system is given by g. The *unconventional, integer* Hall quantization for BLG reads as

$$\rho_H(BLG) = \frac{h}{4Ne^2} \tag{4}$$

where $N = \pm 1$,± 2,... The first LL is therefore 8-fold degenerate, compared to all the remaining LL which are four fold degenerate due to the two electron spins and the two sublattices. [23, 26, 27] In real Hall samples, the discrete Landau levels are broadened into Landau sub-bands due to impurities and phonons[7]. By solving the Schrödinger equation, taking electron scattering into account, two solutions emerge which belong to localized states, and extended states. At zero temperature, the localized states do not carry any current while the extended states do. The transport in the edge channels[8] is ballistic as long as no extended states above E_F are accessible by thermally excited electrons. Occupying these electronic states allows scattering between the forward and backwards edge channels which are otherwise decoupled. The occupation of extended electronic states by thermally excited electrons is best prevented if E_F lies in between two LL which are separated by a large energy gap (high applied B-field) and if the Fermi surface is very sharp (low temperatures). [29, 30] The oscillations of the magneto resistivity with increasing B-field (or V_{BG}) is called *Shubnikov-de Haas (SdH) oscillations.* [31]

[7] At low temperatures where the QHE is observed, the scattering is largely dominated by impurities.

[8] The electronic transport is limited to the edge of the 2DEG, since in the bulk the charge carriers fulfill complete cyclotron circles. At the edge, the charge carriers move in skipping orbits along the edge in so called *edge channels,* in which scattering is strongly suppressed. [28]

2.3 Andreev reflection and Proximity effect

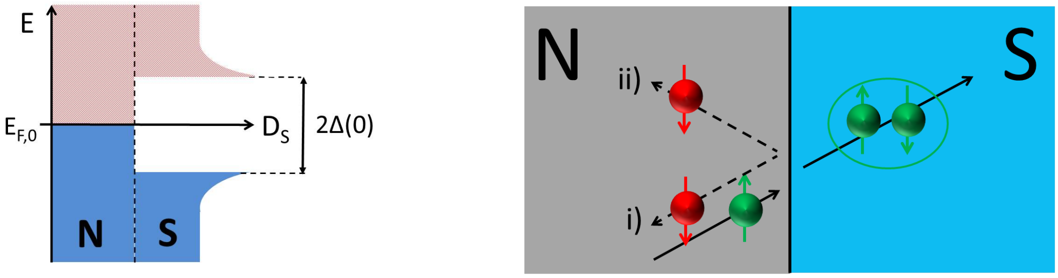

(a) (b)

Figure 3: **a)** Band structure of a SN interface at zero bias across the junction and at zero temperature. Blue indicates the valence band and red hatched indicates the conduction band in the single quasi-particle picture. **b)** An electron (green) coming from the normal conductor hitting the NS interface creates a Cooper pair in S leaving a hole (red) in N. In contrast to most other metals, Andreev retroreflection (i) as well as specular Andreev reflection (ii) can occur in SLG and BLG depending on the energy scale. The probability for a transmission of the electron across the NS interface is τ, while $1 - \tau$ stands for the probability of an ordinary electron reflection at the NS interface.

When two metals are brought into electronic contact, the Fermi levels align themselves in such a way that they are in equilibrium. For both metals the density of states (D_S) at the Fermi energy is non-zero, therefore electrons can be transmitted from one conduction band into another (or holes from one valence band into another). For a SN interface the situation becomes slightly more complicated. In the ground state of a superconductor, the electrons are bound in Cooper pairs and there is an energy gap in the excitation spectrum as shown in fig. 3a. The energy gap is a direct result from the attractive, phonon-mediated electron-electron interaction[9] (electron-phonon coupling) which leads to the condensation of the electrons near the Fermi surface into Cooper pairs.

The transmission of the charge carrier across the SN interface occurs according to two different mechanisms depending on the Fermi energy ($E_F = E_{F,0} + eU$) of the charge carriers.

- $|eU| > \Delta$: If the energy E_F of the incoming quasi-particle in the normal metal is higher/lower than $E_{F,0} \pm \Delta$, the density of states at the Fermi energy is non-zero. Consequently the quasi-particles can be transmitted into the superconductor.
- $|eU| < \Delta$: However, if the energy E_F of the incoming quasi-particle in the normal metal lies within the energy gap of the superconductor $E_{F,0} - \Delta < E_F < E_{F,0} + \Delta$, the transmission of the charge carriers across the SN interface becomes more complex. Quasi-particles cannot be transmitted into the superconductor since the density of states at E_F is zero. It lies in the energy gap of the superconductor. The only possibility for e.g. an incoming electron to be transmitted across the NS boundary into the superconductor is by forming a Cooper pair with a second electron of the normal conductor. The two electrons are taken from opposite corners $\pm k$ of the Brillouin zone, in order to allow the Cooper pair to carry zero total momentum. This corresponds to s-wave pairing, common in conventional superconductors. However, to maintain charge conservation, a hole has to be reflected into the normal metal, as sketched in fig. 3b. Since the electron and hole of the conversion process have opposite charge $\pm e$, a charge of $2e$ is absorbed by the superconductor as a Cooper pair. The returning hole makes an additional contribution to the current, the so called *excess current*. This process is called *Andreev reflection* leading to a doubled conductance $2G$ across the NS boundary in the case of highly transparent contacts. [32, 33] In the normal case the charge carriers are reflected back along the path of the incoming charge carrier, since electron and hole both lie in the conduction band. This type of Andreev reflection is called *Andreev retroreflection*. In fact, the trajectories as well as the magnitude of momentum for the incoming and reflected charge carrier varies slightly. The difference in energy of the incident and reflected charge carrier is absorbed by the Cooper pair. However, the change is much smaller than the momentum itself since the energy of interaction $\sim \Delta$ is much smaller than E_F. [34] It is worth mentioning that a

[9]The electron-phonon coupling dominates the repulsive Coulomb interaction between the electrons.

second type of Andreev reflection exists. In the case of the *specular Andreev reflections*, the angle of the reflected charge carrier has the opposite sign with respect to the incoming charge carrier since the electron from the conduction band is converted into a hole in the valence band. Because the energy difference between electron and hole is in the order of $\sim \Delta$, specular Andreev reflection only becomes relevant for $eU \rightarrow 0$. Specular Andreev reflection shall not be further discussed here as it is of minor importance for the experiments performed in this Master thesis. [33, 35]

When a superconductor is in contact with a normal conductor, which is required for Andreev reflection, proximity coupling occurs. The Proximity effect is known since the pioneering work of R. Holm and W. Meissner. [36] It is based on the fact that the charge carrier cannot change their properties infinitely quickly at the SN interface due to their nonlocality in the metal. Therefore, the Cooper pairs are leaking into the normal metal, before they completely loose their coherence due to scattering events. How far the Cooper pairs leak into the normal conductor is determined by the coherence length of the Cooper pairs and the properties of the normal conductor (e.g. l_{mfp}). For very clean metals as e.g. Cu, the Cooper pairs can penetrate several hundreds of micrometers before they completely loose their coherence. [37] The leaking of Cooper pairs into the normal conductor leads to a modification of the band structure near the SN interface. The energy gap in the superconductor decreases continuously $\Delta_0 \rightarrow \Delta_r$ while approaching the SN interface. On the other hand a small energy gap Δ_i due to the leaking of the Cooper pairs builds up in the normal conductor while approaching the SN interface. [38, 39]

2.4 BKT Theory

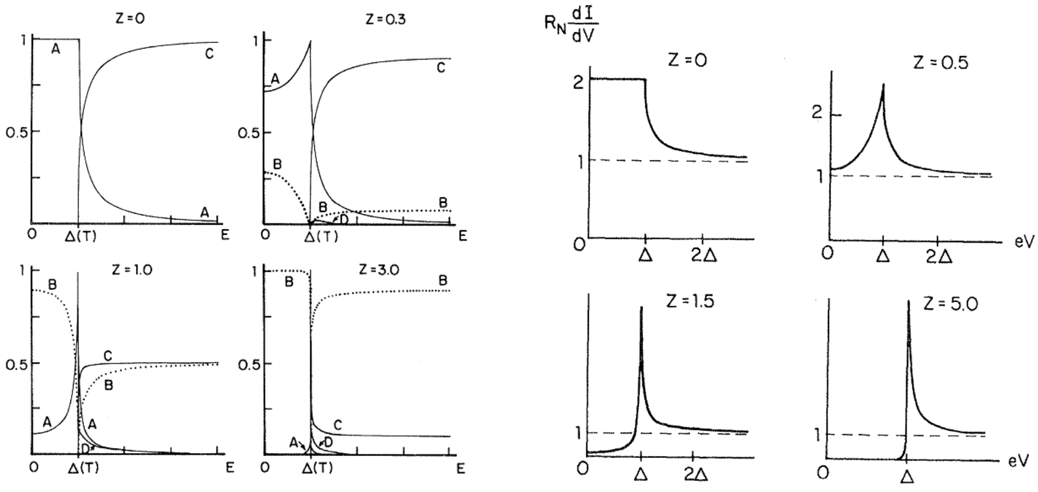

(a) (b)

Figure 4: **a)** Transmission and reflection probabilities of quasi-particles at the SN interface according to the BKT theory. Coefficients for Andreev reflection (A), ordinary reflection (B), transmission without branch crossing (C) and transmission with branch crossing (D) depending on the barrier strength Z at the SN interface. **b)** Resulting conductance across the SN interface at zero temperature. Images from [40].

Blonder, Thinkam and Klapwijk proposed in 1982 a generalized model, known as the BKT theory, to describe the behavior of SN interfaces assuming a generalized semiconductor model. [40] It is based on the Bogoliubov equations [41] to treat the transmission and reflection of particles at the SN interface. By including a tunneling barrier of strength Z in between the SN junction, the IV and $dIdV$ characteristics ranging from tunneling junction to the metallic limit can be modeled.

Particles approaching the SN interface can be transmitted and reflected with certain probabilities, depending on the square amplitudes of the Bogoliubov equation times the corresponding group velocity of the particle. By matching the slope and value of the wave function across the SN junction one can find the probabilities for the following four processes: "A" represents the probability for a Andreev reflection, "B" represents the probability of an ordinary reflection, "C" represents the transmission without branch crossing and "D" the transmission with branch crossing[10]. The modeled probability of these four processes depending on the barrier strength Z can be seen in fig. 4a. In fact, the barrier strength between the SN interface is not the only source for an ordinary reflection. In reality, the Fermi energies of the normal metal and the superconductor are different. This mismatch will cause the establishment of a contact potential which results in some normal reflections, even if no tunnel barrier is present. This effect can be taken into account by simply shifting the Z value to a slightly higher effective value. [42] For Z=0 only Andreev reflection and transmission without branch crossing occur at the SN interface. It shall be noted that Andreev reflection can occur as well for $|eU| > \Delta$ even with a much lower probability. With increasing barrier strength Z the probability for Andreev reflection gradually decreases to zero while the one for ordinary reflection increases towards 1 for $|eU| < \Delta$. However, the probability for Andreev reflection never vanishes at $|eU| = \Delta$, where a peak remains[11]. The conductance, which is the actual measure to be observed in experiments depending on the barrier strength, is shown fig. 4b. For the ideal case, the conductance is doubled for $|eU| \leq \Delta$ while it decreases back to the normal value of 1 for $|eU| >> \Delta$. [40]

[10] Transmission through the interface without branch crossing means that the wave vector is on the same side of the Fermi surface, e.g. $q^+ \rightarrow k^+$, while for a transmission with branch crossing $q^+ \rightarrow -k^+$ is valid.

[11] According to the BKT theory, the position of the two peaks in the conductance gives the gap value of the superconductor only for large values of the scattering barrier. For intermediate values of Z, these peaks occur at energies slightly below Δ.

3 Materials and Methods

3.1 Layered materials

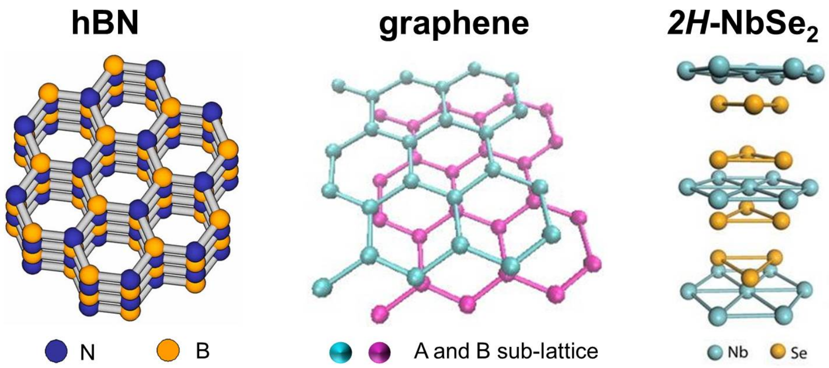

Figure 5: Stacking fashion of the hexagonal, layered materials used in the devices. Hexagonal boron nitride maintains an AAA stacking where boron and nitrogen atoms are alternately stacked on top of each other. The normal stacking order of graphite, and therefore as well of BLG, is ABA (Bernal stacking). The unit cell of *2H*-$NbSe_2$ consists of two sandwiches of Se-Nb-Se. Pictures taken from [43],[44] and J. Hoffmann (group homepage, Harvard Univesity).

The devices built up in this Master thesis were of mainly hexagonal, layered materials such as the insulating hexagonal boron-nitride (hBN), the normal conducting graphene and the superconducting *2H*-$NbSe_2$[12]. The crystal structure of each of them is shown in fig. 5. All three materials are characterized by strong intra-layer bonds but relatively weak inter-layer bonds which allow micro-mechanical exfoliation in order to obtain flakes which are atomically flat and extremely clean with respect to their surface. As a consequence, they can be stacked on top of each other in order to establish high transparency SN junctions. Compared to sputtering, which is required for some non-layered superconductor, no high energetic atoms which might damage the fragile SLG/BLG are involved.

hBN The hBN flakes were used in between the SiO_2 and the graphene to increase the charge carrier mobility, since thermally grown SiO_2 has a significantly higher surface roughness and a higher potential fluctuation due to trapped ions compared to hBN. Furthermore, a thin layer of hBN was used to encapsulate the graphene Hall bar. The defect rate of the ultra pure single crystal hBN used in this report, which were synthesized as described in Ref. [46], is surprisingly low. The reason lies not only in the nature of the material itself, but also in the vast experience these authors gained synthesizing hBN over the last decades.

Graphene High quality kish graphite was used for exfoliation. All the devices fabricated were established of BLG.

[12] There exist different polytypes of $NbSe_2$, which belong to different space groups. Besides the *2H*-$NbSe_2$ there also exists a *4H*-$NbSe_2$ with T_C=6.5 K and T_{CDW} ~42 K. [45] Since only *2H*-$NbSe_2$ was used in this report, it shall be referred to as $NbSe_2$.

Superconductor The use of layered superconductors is of interest since many of them possess interesting physical properties such as[13]: i) A high critical temperature as e.g. observed in the families of BSCCO, TBCCO, YBCO (all belong to the high temperature superconductors). ii) They often belong to the type-II superconductors. Therefore vortex states are present in between the critical fields H_{C1} and H_{C2}. iii) Many of them, such as the transition metal dichalcogenides or YBCO, undergo a *Peierls transition* at T_{CDW} to form charge density waves[14] (CDW). The properties of $NbSe_2$, which was used as superconducting lead, shall be discussed in more detail in the following chapter.

Besides these layered materials, a Si/SiO_2 wafer with a 300 nm thick thermally grown oxide layer was used as a gate dielectric and as a support for the devices. The normal conducting contact leads were made mainly of gold.

3.2 $NbSe_2$

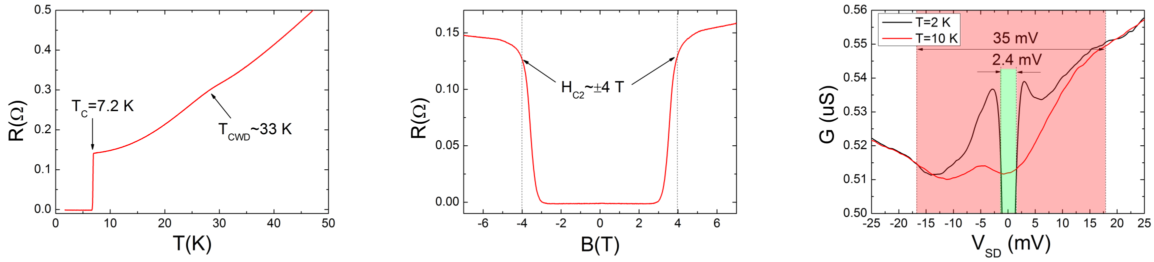

(a) (b) (c)

Figure 6: Characteristics of $NbSe_2$ measured in a MLG-$NbSe_2$-MLG device structure as shown in fig. 17a. **a)** Temperature dependence of the resistance. At T_{CDW} ~33 K the metal undergoes a CDW transition, while at T_C ~7.2 K it becomes superconducting. **b)** Magnetic field dependence of the resistance at T_C=2 K. **c)** 2-terminal measurement of the conductance across a graphite-$NbSe_2$ junction at 2 K and 10 K. The energy gap 2Δ=2.44 meV and $2\Delta_{CDW}$ ~35 meV are indicated in green and red respectively.

$NbSe_2$ belongs to the family of the transition metal dichalcogenide. It is a layered crystal which typically cleaves between the weakly coupled neighboring Se-layers. $NbSe_2$ is a prototypical anisotropic s-wave superconductor below a temperature T_C=7.2 K (see fig. 6a) which allows the use of a simple ^{4}He gas flow cryostat. Furthermore it undergoes a phase transition to an incommensurate[15], triangular charge density wave phase at a temperature T_{CDW} ~33 K. [45, 47] $NbSe_2$ is a type-II superconductor. The resistivity remains zero up to a magnetic field of ~3 T, above which it starts to increase to ~5-6 T where it saturates (values comparable to the ones at 10 K). The non-zero resistivity below $H_{C2}(2K)$ ~4 T is understood in terms of the diffusion of the vortices across the superconductor and is called *flux-flow resistance*. On the other hand, a non-normal resistivity above H_{C2} can be attributed to fluctuations of the superconductor. Another interesting property of $NbSe_2$ is the existence of surface superconductivity above H_{C2} on the lateral edge of the crystal. This phenomenon was previously observed for $NbSe_2$ up to critical fields of $H_{C3}(2K)$=1.6-1.7H_{C2} ~6.7 T. [48] $NbSe_2$ has two energy gaps of 2Δ=2.44 meV and 2Δ=2.26 meV depending on the k-vector since the CDW breaks the symmetry of the hexagonal crystal structure. The energy gap of the charge density wave band is $2\Delta_{CDW}$ ~35 meV. The energy gaps 2Δ=2.44 meV and $2\Delta_{CDW}$ are indicated in fig. 6c. [47]

[13] The following list shall not be considered to be complete. It rather is a selection of some interesting properties many layered superconductors have.

[14] A charge density wave is a periodic modulation of the electronic charge density. Its existance was first predicted by R. Peierls in 1930.

[15] Incommensurate are materials which possess perfect long range order but which lack translational periodicity in one or more of their lattice directions.

3.3 Fabrication of the devices

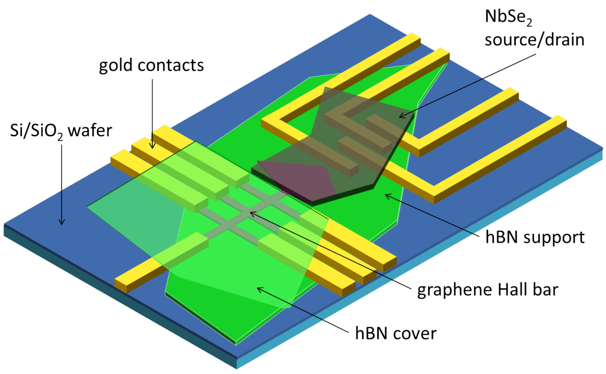

(a)

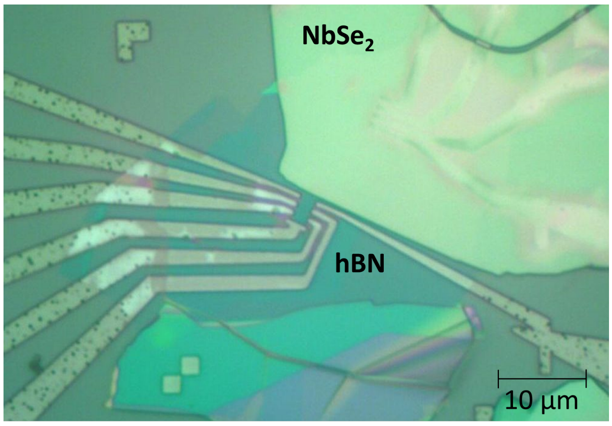

(b)

Figure 7: **a)** Sketch of the final graphene Hall bar on the hBN support. It is contacted with several gold, and one $NbSe_2$ lead. The Hall bar is encapsulated with a thin layer of hBN to protect it from environmental influences. **b)** Optical image of a finished device which is ready to be measured.

In the following, the most critical steps required to produce the device sketched in fig. 7a are given. In fig. 7b an optical image of a finished device is shown. For a more detailed description of the fabrication of the devices the reader is referred to the author's Projectwork chapter 3.2.

1. Transfer of a BLG onto a ~40 $nm\pm$ 20 nm thick hBN support, which itself is located on the piranha cleaned Si/SiO_2 wafer. The use of a ~40 $nm\pm$ 20 nm thick hBN dielectric allows an effective shielding of the SiO_2 potential fluctuation and a smoothing of its rough surface, while not breaking the gold contacts on the hBN edge which will be evaporated as described in step 2. For all the transfers performed a micro-manipulator mounted on an optical microscope was used. After completed transfer the sample was annealed in H_2/Ar atmosphere at 300 °C for 3 h to remove resist residues[16]. After annealing, the surface quality of the graphene on top of the hBN support was checked using an AFM microscope.

2. Standard E-beam lithography and E-beam evaporation was used to write and evaporate the electric contacts (1 nm Ti + 10 nm of Pd + 70 -100 nm Au). The layer of Pd reduced detachment of the contacts from the devices with a hBN support while annealing.

3. Standard E-beam lithography was used to write the etching pattern for the graphene Hall bar. The graphene was etched using an oxygen plasma etcher. Annealing of the device.

4. The graphene Hall bar was encapsulated with a thin, protective layer of hBN. However, an overlap area in order to establish the SN interface was left out. After completed transfer, the device was annealed to ensure a clean contact area for the $NbSe_2$.

5. Before transferring, the $NbSe_2$ flake was scanned with an AFM microscope to ensure a clean surface. The chosen $NbSe_2$ flakes had a thickness of approximately 50 nm, which ensured chemical stability due to passivation while maintaining its flexibility. [49] After the completed transfer the PPC layer was left on the device because dissolving $NbSe_2$ in chloroform might change its properties and annealing will certainly destroy its superconducting properties.

[16] These settings were used for all the annealing steps needed to complete this device

3.4 Measurement setup

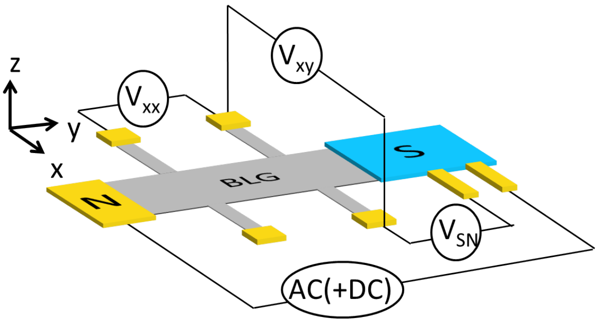

Figure 8: Measurement setup with a 4-terminal measurement of the magneto resistance (V_{xx}), Hall resistance (V_{xy}) and the SN resistance (V_{SN}). Injection of either AC or AC+DC current.

The measurements were performed in a variable temperature insert (VTI) cryostat which can provide a base temperature of ~1.7 K and a magnetic field up to 8.8 T[17]. The current biased, differential conductance ($G = dI/dV$) across the SN junction was measured with low frequency (~17 Hz) standard lock-in technique in the presence of both, a small AC excitation current superimposed on a DC bias current. QHE measurements were taken at zero DC current. A sketch for the 4-terminal measurement setup is shown in fig. 8.

[17]Some of the control devices were measured with a PPMS system, providing a base temperature of ~2 K and a magnetic field up to 14 T.

4 Results and Discussion

4.1 Characterization of the device

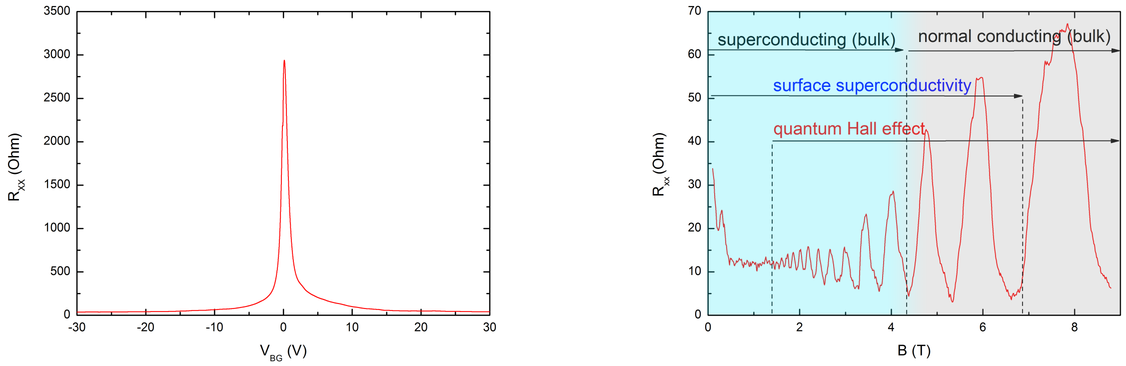

(a) (b)

Figure 9: Quality measurements of the BLG after current annealing. **a)** The charge neutrality point was found to be at V_{BG}=0.1 V with a charge carrier mobility of μ=110'000 $cm^2V^{-1}s^{-1}$ (n_e ~1.2*10^{12} cm^{-2}, V_{BG}=40 V). **b)** SdH oscillations were observed starting at ~1 T at a hole density of n_h ~1.2*10^{12} cm^{-2}, V_{BG}=-40 V. Furthermore, the relevant electronic states of $NbSe_2$ as well as the onset of the SdH oscillations are given.

4.1.1 Graphene

The quality of the graphene was investigated in multiple ways. The narrow width of the Dirac peak and the high charge carrier mobility (μ=110'000 $cm^2V^{-1}s^{-1}$ at n_e ~1.2*10^{12} cm^{-2}) both indicate low disorder in the graphene (see fig. 9a). It has to be mentioned that the effective mobility of the charge carriers might be higher as calculated with the formula

$$\mu = \frac{L}{W}\frac{1}{nR_{xx}e} \tag{5}$$

where L and W are the dimensions of the Hall bar, e is the electron charge and n is the charge carrier density. The latter was obtained from the SdH oscillations according to $n = \frac{2e}{h}\frac{i-j}{1/B_i - 1/B_j}$, where h is the Plank's quantum and i,j are the number of the peaks in magneto resistance[18]. The error might occur, because equation (5) was derived from the Drude formalism, which assumes diffusive electrical transport, while in the devices produced it is reasonable to assume quasi ballistic transport . Therefore scattering events at the SN and NN interfaces are most probably dominating over the scattering events within the graphene Hall bar itself. By increasing the length of the Hall bar and the distance between the sensing electrodes for R_{xx} the effective mobility might be measured more accurately since the scattering events within the graphene begin to dominate the scattering at the SN and NN interfaces. The charge neutrality point at V_{BG}=0.1 V indicates a high purity level of the graphene[19]. The pronouncement of the SdH oscillations and its first appearance with increasing magnetic field (onset at $B \sim 1$ T as shown in fig. 9b) reveals information about the disorder in the system by probing the density of states. In a system with low disorder, the LL's are narrow. Therefore, a significant variation of the magneto resistance becomes relevant at lower magnetic field compared to a system with higher disorder (wider LL's).

[18]The labeling of the peaks in magneto resistance is arbitrary, but $i - j$ of neighboring peaks must be 1.
[19]In the absence of any doping the Dirac peak is positioned at zero back-gate voltage.

4.1.2 SN interface

The quality of the SN interface was characterized by measuring the 4-terminal resistance across the SN interface. The SN contact resistance was found to be in the order of $R_{graphene-NbSe_2}$ ~300-1000 Ω. Measuring the temperature dependance of the SN resistance gave additional information about the tunnel barrier which typically exists at the SN interface. The presence of a tunneling barrier, e.g. a thin oxide layer between the normal- and the superconductor, causes an increase of the resistance at low temperature, where the tunnel barrier dominates over the intrinsic resistance of the materials. This effect, which is called the re-entrance effect, is most dominant below T_C where the intrinsic resistance of the superconductor vanishes. [50, 51] In our sample a moderate re-entrance effect was observed. Because current annealing steps were performed occasionally in between the measurements, the effective value of the SN interface resistance and the re-entrance effect varied slightly with it. Current annealing was performed at room temperature, where all the involved materials, especially the covering PPC, were most flexible. It was found to be most successful when short current pulses (~5 s) of up to 1.5 $mA/\mu m$ were applied. This way the overall mobility in graphene could be increased and he contact resistance of the SN junction could be decreased to values as low as ~300 Ω. Longer (~5 min), but less intense (<1 $mA/\mu m$) current annealing turned out to be less effective. After current annealing, the sample was held at room temperature for approximately one hour in order to allow complete discharging. By not doing so, the Dirac peak showed a hysteresis like behavior at low temperature due to frozen out charge carriers trapped in the device.

4.1.3 Co-existence of SC and QHE

As shown in fig. 9b, the first SdH oscillations appeared at around $B \sim 1\ T$, while the bulk superconductivity remains until ~4 T. This leaves a window of ~3 T within which both effects are co-existing.

4.2 Temperature dependent differential conductance across the SN junction

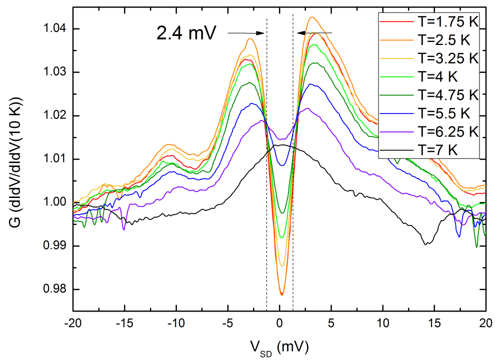

Figure 10: Normalized differential conductance ($T/10K$) across the SN interface for different temperatures (T= 1.75-7 K) at n_h ~2.9*10^{11} cm^{-2}, V_{BG}=-10 V.

The normalized differential conductance ($T/10K$) across the SN interface was measured at different temperatures, shown in fig. 10. The width of the zero bias dip in the differential conductance is the signature of the superconducting energy gap, as shown by Sheet *et al.* [52] The deviation in width of the zero bias dip from the expected literature value, indicated with dashed lines, is rather expected as demonstrated in previous PCARS experiments. [53, 54] The amplitude of the Andreev reflection structure is greatly depressed (signal-to-background ratio of $\leq$5%), indicating a weak superconductor/graphene coupling[20]. However, this ratio is comparable to the best signal-to-background ratios obtained for graphene/superconductor junctions. [55] Both effects, the spread in energy and the depressed signal-to-background amplitude can be attributed mainly to the reduction of the quasi-particle lifetime, resulting from, e.g., inelastic quasi-particle scattering near the SN interface (surface degradation, contamination, ect.). [54]

4.2.1 Thermal heating effects at the SN point contacts

Besides the enhanced differential conductance and the zero bias dip at V_{SD}=0 mV, there were several additional dips visible in the differential conductance, as indicated with arrows in fig. 11a. There are two models proposed to explain the origin of these additional dips which are frequently observed in point contact Andreev reflection spectroscopy (PCARS). [52, 56] In the local heating model it is the effective contact area between the point contact probe and the superconductor which greatly influences the shape and position of these dips. However, the physical explanation for their overall existence is given by the critical current density of the superconductor at the point contacts. As soon as the critical current density is exceeded, the resistivity of the superconductor rapidly increases to its normal value, therefore causing a dip in the differential conductance. [52]

The point contact resistance between the superconductor and the normal conductor can be divided mainly into three regimes, depending on the ratio between the mean free path of the charge carriers in the normal conductor (l_{MFP}), and the radius of the contact area (r, assuming a circular contact area).

Ballistic regime In the ballistic regime, where $l_{MFP} >> r$, electrons can accelerate freely within the point contact area without being scattered (no heat dissipation). The contact resistance contributes the dominant part of the resistance in the circuit. The resistance in such a situation was calculated by Sharvin and equals to $R_S = (4\rho l_{MFP})/(3\pi r^2) = 2h/(erk_F)^2$ where ρ is the resistivity of the normal conductor.

[20] Similar tendencies were observed in multilayer graphene (MLG) - $NbSe_2$ control devices. The corresponding curves can be found in the supporting material.

Diffusive regime In the diffusive regime, where $l_{MFP} << r$, the electrons crossing the interface undergo many inelastic scattering events. As a consequence, power gets dissipated in the contact region (joule heating) leading to an increase of the effective temperature at the point contact compared to the rest of the environment. The Maxwell resistance is given by $R_M = \rho(T_{eff})/2r$ where $\rho(T)$ is the bulk resistivity and T_{eff} is the effective temperature of the point contact. Since $R_M \propto 1/r$ whereas $R_S \propto 1/r^2$, the Maxwell resistance decreases more rapidly than the Sharvin resistance with increasing contact area.

Intermediate regime In the intermediate regime the resistance is not dominated by either R_S or R_M. The resistance can be expressed by a simple interpolation formula derived by Wexler $R = R_S + \Gamma(K) * R_M$, where the Maxwell resistance is multiplied by a function $\Gamma(K)$ of the Knudsen ratio[21] K. [52, 54, 57]

The ratio R_M/R_S influences the position and amplitude of the peaks in the differential conductance.

- **Position:** The position of the peak in the differential conductance can shift with temperature, because the critical current depends on T. The effective temperature at the point contacts is given by $T_{eff} = T_{cryostat} + T_{joule\,heat}$. Therefore T_{eff} can be changed in two ways: i) Varying $T_{joule\,heat}$, which equals to a change of the ratio R_M/R_S, can be achieved by ,e.g., current annealing, where the effective contact area is altered. ii) Varying $T_{cryostat}$ which is the temperature of the cryostat.
- **Amplitude:** The amplitude of the dip is absent in the ballistic regime and becomes more pronounced with increasing ratio of $R_M/R_S \propto r$. However, in the case of very large-area, low-resistance contacts (R_M/R_S>>1), joule heating will drive the superconductor into the normal conducting state before the current reaches the critical value. Therefore no additional dips will be observed in the differential conductance. [52, 53]

It shall be emphasized that with this model only dip 1, in fig. 11a can be explained, since the transition from the superconducting to the normal conducting regime occurs only once. So far no model which could explain the multiple dips completely satisfying was found.

[21] The Knudsen ratio is a dimensionless number defined as the ratio of the mean free path to a representative physical length scale, e.g. the radius of the point contacts.

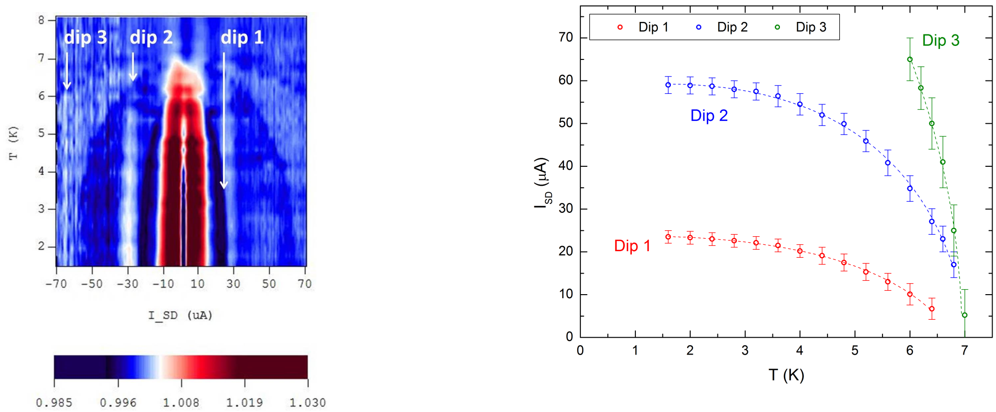

(a) (b)

Figure 11: **a)** The color plot of the normalized differential conductance clearly reveals a shift in energy ($E_{dip} \propto I_{SD,\,dip}$) of the additional dips outside the superconducting energy gap with temperature. **b)** The evolution of the dip position with temperature fitted according to equation (6).

While the position of the Andreev reflection peaks was relatively constant in between the current annealing steps, the position of the additional dips revealed significant changes which indicates a modified ratio of R_M/R_S. [53, 54] The evolution in energy ($E_{dip} \propto I_{SD,dip}$) of the additional dips for a chosen data set, shown in fig. 11b, revealed a BCS gap-like trend[22]. The data was fitted with

$$I_{SD,dip}(T) = A\left(1 - \frac{T}{T_C}\right)^{1/2} + B + C(T_C - T) \tag{6}$$

which approximates the BCS gap-like behavior[23]. The critical current ($I_C = I_{SD,\,dip\,1}(T)$) was found to scale proportional to the superconducting energy gap with temperature. The same behavior was observed for the dips 2 and 3, relating them as well to the superconductor. However, all these features are not generic features of the superconductor. Similar observation were made in related studies. [53]

As a matter of fact, the size of the effective contact area is not directly related to the apparent contact area of the point contacts. One possibility to estimate the effective contact area is to use the relation $I_{SD,\,dip\,1}(T = 0K) = j_C A$, where $I_{SD,\,dip\,1}(T = 0K)$ ~20 μA is the critical current (current at dip 1 where the transition from the superconducting to the normal conducting regime takes place) extracted from fig. 11b, j_C ~1 Acm^{-2} is the critical current density[24] of $NbSe_2$ and A is the effective contact area. [48, 52, 59, 60, 61] The calculated effective contact area is then in the order of 1 μm^2.

Alternatively, the effective contact area, assuming a completely ballistic (Sharvin formula[25]) or a completely diffusive (Maxwell formula[26]) charge carrier transport across the SN interface leads to $A_{Sharvin}$ ~0.0001 μm^2 and $A_{Maxwell}$ ~0.01 μm^2. Since $A_{Maxwell}$ is much closer to the result obtained using the critical current density ($I_{SD,\,dip\,1}(T = 0K) = j_C A$) the SN junction in our sample is much more likely to be in the diffusive regime rather than the ballistic regime.

[22] In the BCS theory the evolution of the energy gap is given by $2\Delta(T) \approx 3.52 k_B T_C \left(1 - \frac{T}{T_C}\right)^{1/2}$ for $T \sim T_C$, while it has a linear behavior for $T \to 0$. [58]

[23] The first term ensured the BCS like behavior for $T \sim T_C$ while the last two terms account for a linear behavior at low temperatures $T \to 0$. The last two terms were not derived directly from the BCS theory. However, they were chosen in such a way that they imitate its behavior.

[24] The critical current densities for $NbSe_2$ varied over several orders of magnitude depending on the reference. The value chosen appeared to be roughly average.

[25] The values used were R_S ~800 Ω and k_F ~10^6 cm^{-1} at n_h ~$2.9*10^{11}$ cm^{-2} according to [25].

[26] The values used were R_M ~800 Ω and $\rho(T_{eff}) \sim \rho(T)$=65 Ω, which is valid in graphene at low temperatures according to [62].

4.3 Magnetic field dependent differential conductance across the SN junction

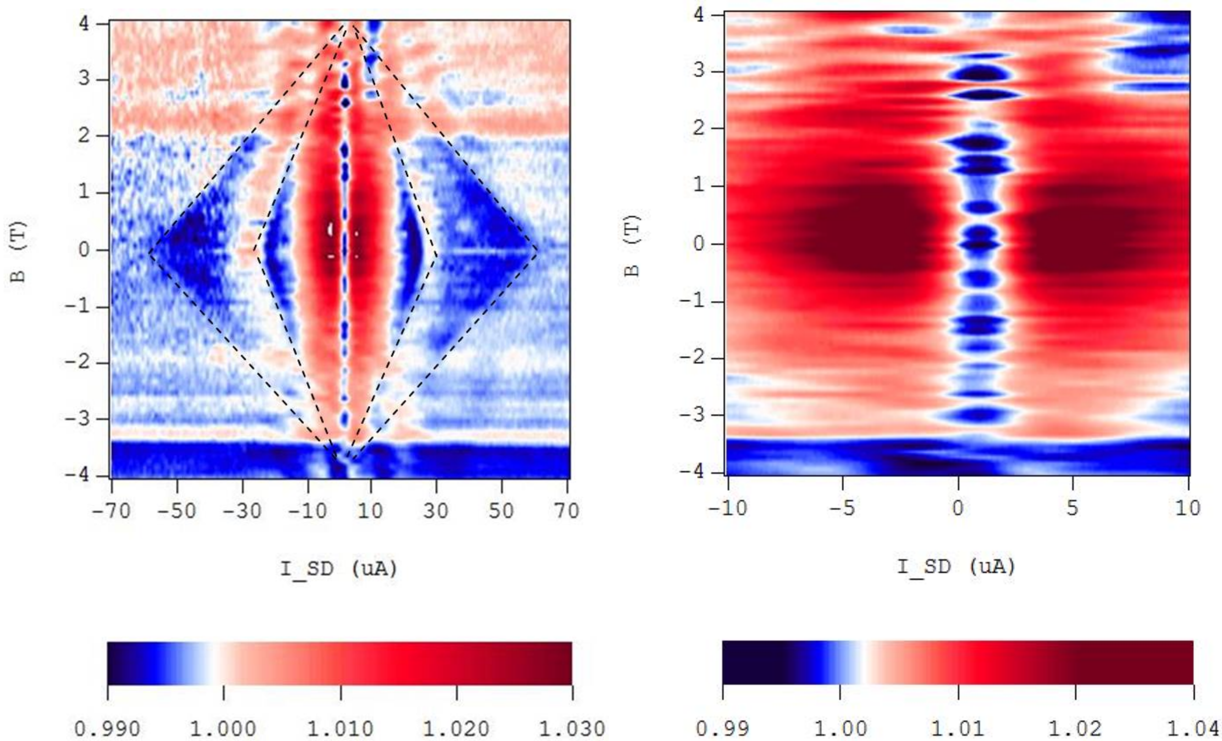

(a) (b)

Figure 12: **a)** The normalized differential conductance (1.7 K/ 10 K) across the SN interface at n_h ~1.45*10^{12} cm^{-2}, V_{BG}=-50 V reveals an almost linear behavior of the additional dips in the differential conductance outside the superconducting gap. The dashed line acts as a guidance for the eye. **b)** The zero bias differential conductance appeared modulated with an oscillating like pattern.

In the magnetic field dependent measurement, the additional dips seemed to scale linear with the magnetic field, as shown in fig. 12a. The dashed line shall act as a guidance for the eye since the exact behavior for $B \rightarrow \pm 4$ T was difficult to distinguish. They are symmetric with respect to the magnetic field and the source-drain current and disappear at $B \sim \pm 4$ T in good agreement with H_{C2} of $NbSe_2$ at T=2 K. [48] Since in the previous chapter it was found that these dips scale proportional to the superconducting gap, it can be concluded that the superconducting gap in $NbSe_2$ seems to depend linearly on the applied magnetic field.

The zero bias dip appeared strongly altered by the magnetic field, seeming to oscillate with it, as shown in fig. 12b. This behavior could clearly be related to the geometry of the device (the Hall bar design and the BLG) because it was completely absent in any MLG-$NbSe_2$-MLG control devices[27]. The oscillating behavior of the zero bias dip shall be discussed in chapter 4.5.

[27]For more details, the reader is referred to the supporting material, fig. 17d.

4.4 Quantum Hall effect with superconducting lead

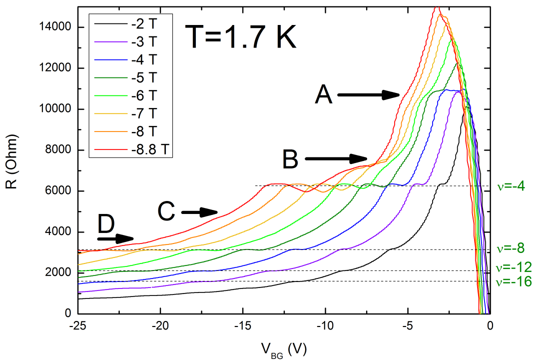

(a)

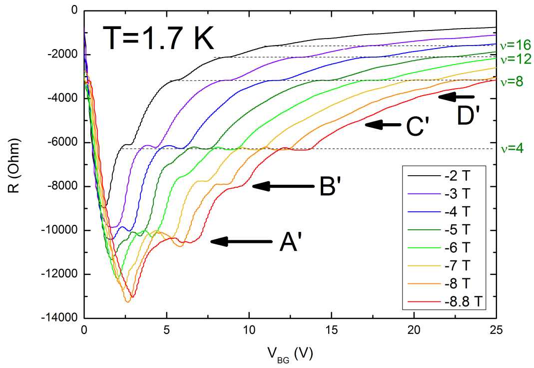

(b)

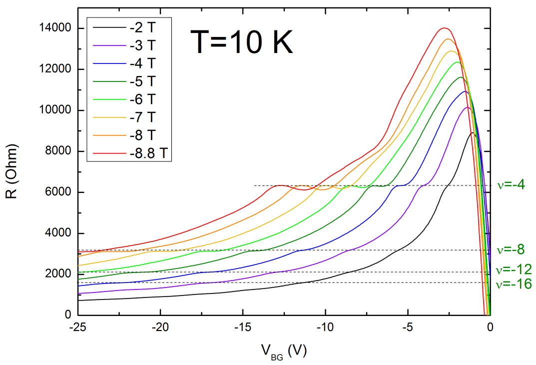

(c)

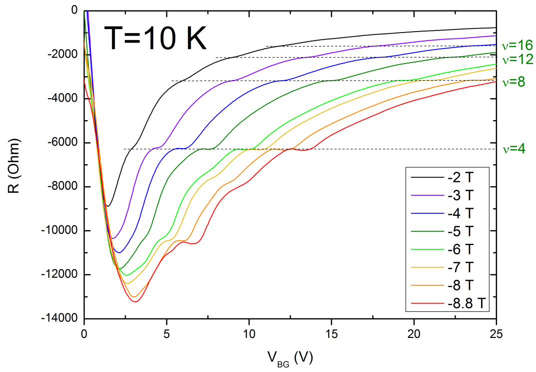

(d)

Figure 13: Quantum Hall measurement in BLG with hole (**a**/**c**) and electron (**b**/**d**) doped region. At T=1.7 K $NbSe_2$ is in its superconducting state (**a**/**b**) while at T=10 K it is in its normal conducting state (**c**/**d**). The most significant differences between the superconducting and the normal conducting state are indicated with arrows.

The measurement taken at T=1.7 K, shown in the first row in fig. 13, represents $NbSe_2$ in its superconducting state while the measurement taken at T=10 K, shown in the second row in fig. 13, is the reference where $NbSe_2$ is in its normal conducting state. The left column in fig. 13 shows the hole doped region while the right column shows the electron doped region. In both measurements, Hall plateaus according to equation (2) appeared at magnetic fields of B ~1 T and spin splitting for these Hall plateaus was observed at magnetic fields as low as ~7 T. These observations underline once more the high quality of the hBN supported quantum Hall bar. The first four Hall plateaus and their filling factors are labeled with dashed lines in fig. 13. It is worth mentioning that for $B < H_{c2}$, where $NbSe_2$ is superconducting, the Hall resistance was slightly modified in its absolute value (reduced by ~1%) as compared to $B > H_{c2}$, where $NbSe_2$ is in its normal conducting state. However, this effect shall not be further discussed as it is beyond the scope of this Master thesis.

By comparing the first and second row of fig. 13, several additional features were observed. The most striking ones are labeled with A/A', B/B', C/C' and D/D' in the hole/electron doped region respectively. Without doubt the most significant feature is labeled with A/A'. Interestingly, it is not symmetric in all belongings for the electron and hole doped region. While at 10 K it is absent for V_{BG}<0, it is partially present at V_{BG}>0. Furthermore, plateau A exists only up to B ~6.5 T, after which it mostly disappears, while plateau A' remains present up to 8.8 T. The observation of plateau A' up to 8.8 T excludes superconductivity as a cause for its appearance. However, for plateau A superconductivity cannot be completely excluded if one considers the existence of surface superconductivity since the latter was observed in $NbSe_2$ until ∼6.5 T at 2 K. [48] Nevertheless it has to be stressed that so far no proof for or against the observation of surface superconductivity in this sample has been found.

The feature labeled in B/B', C/C' and D/D' are equally present in the electron and hole doped region. All of them are most pronounced at high magnetic field (B=8.8 T) and at low temperature (1.7 K) which again excludes superconductivity as a cause for their appearance. It is misleading that the features C/C' and D/D' seem to be absent at 10 K, since most probably it is the thermal smearing which is responsible for the vanishing of those weak features at higher temperatures. This conclusion is supported by the behavior of plateaus B/B', which both clearly remain at 10 K.

The fan plot diagram of the normalized magneto resistance, shown in fig. 14, reveals more additional plateaus than the one indicated in fig. 13. The ones given in equation (2) are labeled in green (R_{xx}=0) while the additional ones are labeled in violet(R_{xx} ≠0)[28]. Since all the Hall plateaus labeled in violet, with ν=-2 as an exception, were found not to be related to superconductivity, their exact cause was not investigated further. Furthermore, for ν=-2, which is the only questionable filling factor, further investigation were beyond the scope of this Master thesis.

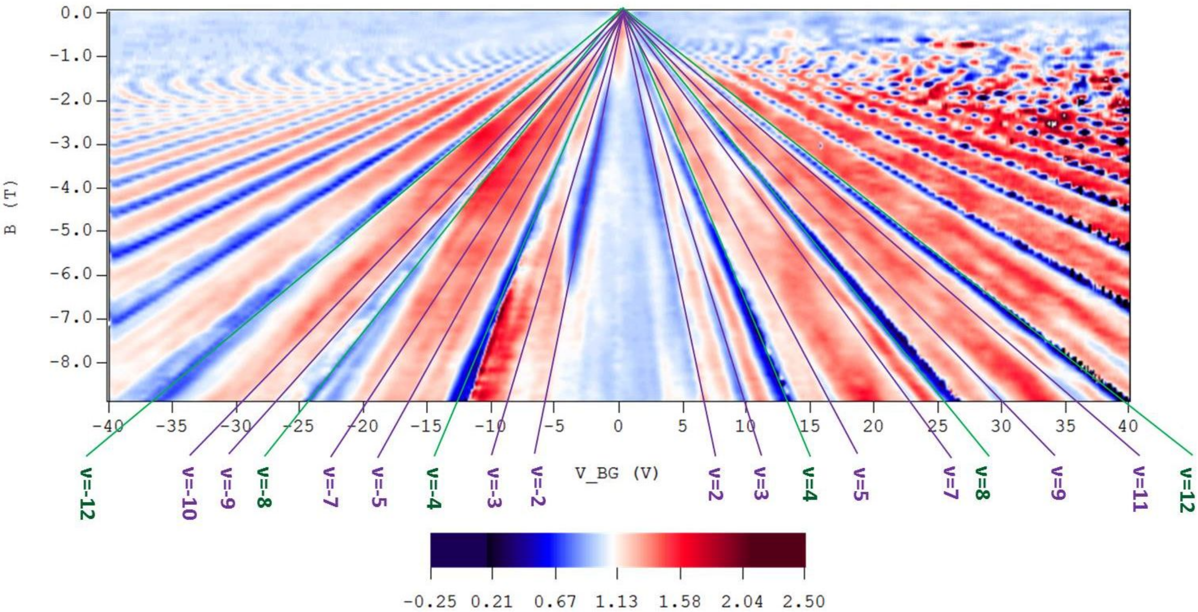

Figure 14: Fan plot diagram of the normalized magneto resistance (1.7 K/10 K). Green indicates filling factors where the corresponding magneto resistance is zero while violet indicates the filling factors where the magneto resistance was non-zero.

[28]Only filling factors $\nu \leq \pm 12$ are labeled in fig. 14.

4.5 Modulated zero bias resistance with magnetic field

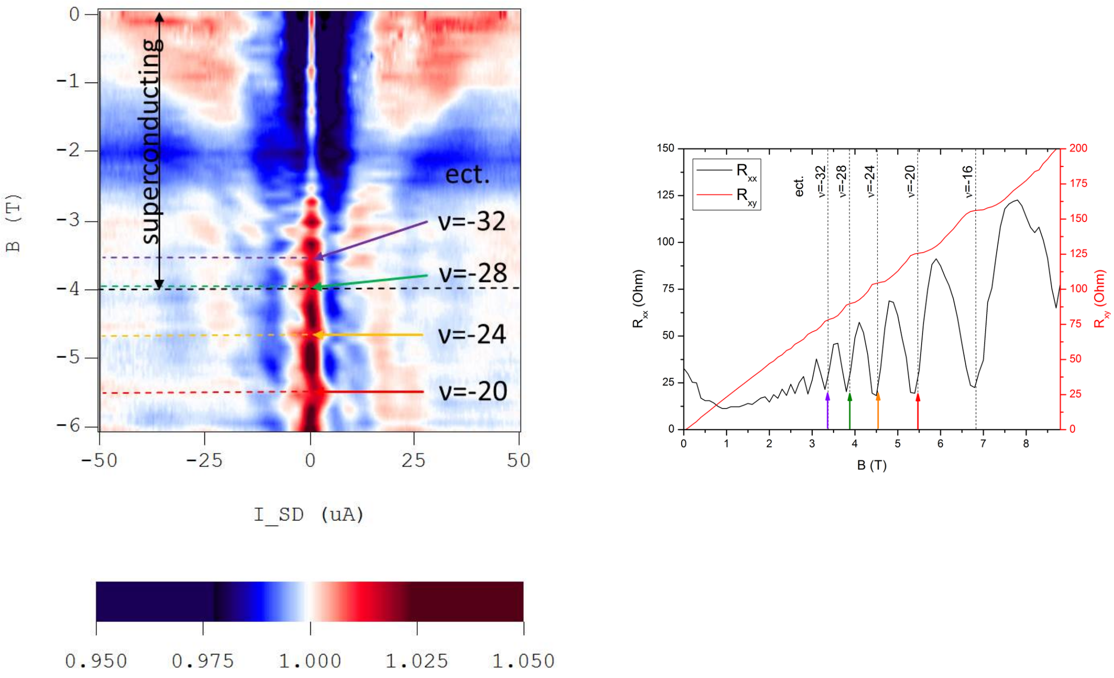

(a) (b)

Figure 15: **a)** The minimum (see colored arrows) and maximum in the oscillation like behavior of the normalized zero bias resistance (1.7 K/10 K) across the SN junction could be related to incompressible and compressible states of the QHE. The corresponding filling factors to the first four minima are indicated with colored arrows. **b)** SdH oscillations of the magneto resistance (black) and Hall resistance (red) with varying magnetic field. Both measurements, shown in the color plot and QHE data, were taken at a charge carrier density of n_h ~1.16*10^{12} cm^{-2}, V_{BG}=-40 V.

By measuring the normalized differential resistance across the SN junction (R_{SN}), an oscillation like behavior of the zero bias peak[29] was observed as shown in fig. 15a. The evolution of the zero bias resistance with the magnetic field was cross-referenced with the data from the quantum Hall measurement, namely the evolution of the magneto resistance and the Hall resistance with increasing magnetic field, as shown in fig. 15b[30]. The minimum in the zero bias resistance could clearly be related to incompressible states of the QHE, as indicated with colored arrows in fig. 15a and fig. 15b, while the maximum could be related to the compressible states. Typically, incompressible states are characterized by a zero magneto resistance (and a plateau of the Hall resistance), which indicates topologically protected edge channels. The magneto resistance in fig. 15b did not completely drop to zero, which indicates that some limited scattering events remained. On the other hand, the compressible states are characterized by a maximal magneto resistance and a Hall resistance located in between two different plateaus. Furthermore it was possible to assign the filling factor to the corresponding minimum of the zero bias resistance as indicated in fig. 15a.

For magnetic fields smaller than H_{C2} the superconducting gap is non-zero allowing the co-existence of superconductivity and the quantum Hall state. For the incompressible states with $B \leq 4$ T, Cooper pairs are injected into the edge channels only. Because in the compressible states the edge channels are not topologically protected any more, the conductivity across the sample is carried by the bulk (diffusive transport) and the edge channels (ballistic transport). Consequently Cooper pairs can be injected as well in the bulk of graphene.

[29] So far always the differential conductance was measured across the SN interface, having a zero bias dip rather than a zero bias peak. However, in this measurement the differential resistance was more convenient because the zero bias peak oscillations were cross-referenced with the measurement from the QHE, which is typically given in resistance.

[30] The data shown in fig. 15b was extracted from a set of line traces of R_{xx} vs. charge carrier density (typical QHE measurement, B=$const.$ for each line trace). Since the number of line traces taken was significantly smaller than the number of data points taken per line trace, the given plot is rather rough. However, the SdH oscillations and the quantum Hall plateaus are pronounced enough to distinguish between compressible and incompressible states of the QHE.

5 Conclusions

For the first time a quantum Hall bar made out of BLG was coupled to a layered superconductor, namely $NbSe_2$. The exfoliation and stacking method, including hBN as an ultra clean and flat dielectric, allowed the establishment of high quality quantum Hall devices (μ=110'000 $cm^2V^{-1}s^{-1}$ at n_e ~1.2*10^{12} cm^{-2}, Dirac peak off-set of V_{BG}=0.1 V, first SdH oscillations observed at ~1 T) with a transparent SN interface ($R_{graphene-NbSe_2}$ ~300-1000 $Ohms$).

The general shape of the differential conductance across the SN junction could be well explained with the BKT theory. The maximal enhancement of the differential conductance due to Andreev reflection was in the order of ~5% at T=1.7 K, which indicates a relatively weak coupling between $NbSe_2$ and the graphene. However, this is comparable to the best signal-to-background ratios obtained for the coupling of a superconductor to graphene so far. Additonal dips in the differential conductance outside the energy gap could be related to the Maxwell resistance, which dominates the SN interface resistance. Even though these additional dips were found to scaled proportional to the superconducting energy gap, they are not generic features of the latter.

By measuring the Hall resistance in the QHE, clearly pronounced plateaus were observed. Furthermore additional filling factors with a non-zero magneto resistance appeared. However, most of them were found not to be related to the superconducting lead. The only exception, where the question remains open if surface superconductivity is involved or not, is filling factor ν =-2 which disappeared at B ~6.5 $T \sim H_{C3}$. However, so far no proof for or against the observation of surface superconductivity in the sample measured has been found.

The oscillation of the zero bias peak in the differential resistance across the SN junction were related to compressible and incompressible states of the QHE. A minimal zero bias peak was found to belong to an incompressible state while a maximal resistance belongs to a compressible state of the QHE. Furthermore it was possible to relate each dip in the zero bias resistance to its corresponding filling factor.

6 Outlook

The following outlook is split into three subsections ordered in terms of the required effort to adjust the device.

6.1 Transverse magnetic focusing

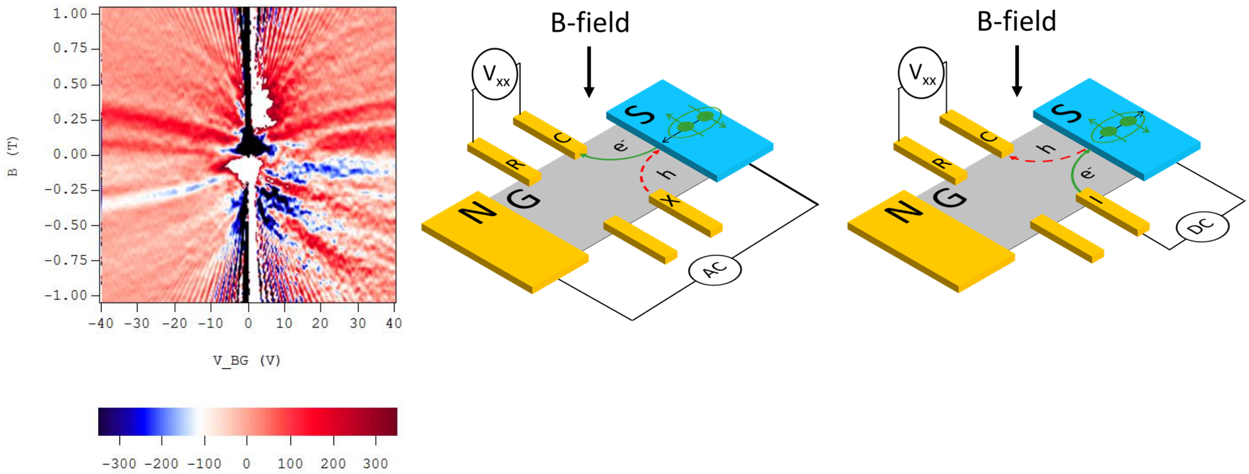

(a) (b) (c)

Figure 16: **a)** Signature of TMF in the magneto resistance $d^2G/(dBdV_{BG})$ at low magnetic fields (B <1 T) for the measurement setup sketched in (b). **b)** The electrodes N and S were used as source/drain while C and R were the collector and reference electrode respectively. Since this setup was designed for the QHE measurement, an AC current was applied between N and S. **c)** Sketch of an optimized measurement setup to be used in further measurements. The injection electrode is labeled with I.

By measuring the magneto resistance in the QHE measurement, an effect called *transverse magnetic focusing* (TMF) was observed at low magnetic fields (B <1 T). It is based on the circular motion of the charge carriers in a magnetic field due to the Lorenz force and the large mean free path (l_{mfp} $\sim$1μm) in graphene. [63] Assuming a thin injection and collector electrode, the charge carriers are focused from the injection electrode to the collector electrode only for discrete values of the magnetic field according to

$$B^{(p)} \propto p * \sqrt{n} \tag{7}$$

where $p-1$ is the number of reflections off the edge in the system (e.g. p=1 corresponds to direct injector to collector trajectory without reflections on the sample edge) and n is the charge carrier density ($V_{BG} \propto n$). [63] TMF was observed by measuring the magneto resistance for the QHE, as sketched in fig. 16b. However, this setup was not primarily designed to measure TMF. As a result, the signal suffered from the following limitations: i) Due to the use of AC current S acts as an injection electrode only for half of the period while for the other half of the period N is the injector. Because of the asymmetric device structure none of the charge carrier is focused into the collector for the second half of the period[31]. ii) S is rather wide (1.5 μm) which causes a smearing of the signal. An improved measurement setup is sketched in fig. 16c. With this configuration, TMF can be investigated under the influence of Andreev reflection. First test revealed a difference in signature depending on whether the $NbSe_2$ is in its superconducting or its normal conducting state. The setup configuration sketched in fig. 16c is only one of many possible configurations to investigate TMF including a superconducting lead. For the TMF measurements there is no change of the device design required at all.

[31]The distances between the electrodes N&R and S&C are not equivalent.

6.2 Influence of vortex states on the QHE

By topping the Hall bar devices with $NbSe_2$ the influence of the Meissner state (B=0-H_{C1} where the magnetic field is completely screened) and the Shubnikov phase (B=H_{C1}-H_{C2} where the superconductor is penetrated by Abrikosov vortices) on the signature of the Hall effect and the quantum Hall effect can be investigated. The classical Hall effect (e.g. by using graphite instead of SLG/BLG) might be of interest since the results are most probably easier to understand compared to the QHE which is much more complex. This experiment involves only a small adjustment to the pre-existing device structure because the graphene Hall bar is already encapsulated with a thin top layer of hBN and therefore one can cover the Hall bar directly with an additional, thin layer of $NbSe_2$.

6.3 Superconductor with stronger coupling to graphene

Even though the signal-to-noise ratio of $NbSe_2$ to graphene was found to be comparable with the best graphen/superconductor junctions available so far, it is still characterized by a relatively weak coupling. By using other layered superconductors this ratio might be increased. An alternative superconductor has to satisfy several requirements, such as: 1) Easy to cleave with a clean surface. 2) Good contact properties and a stronger coupling with graphene as compared to $NbSe_2$. 3) Chemically stable in air (at least for a certain period of time). Furthermore higher H_{C2} and larger 2Δ as compared to $NbSe_2$ would be highly desirable. Possible candidates belong to the family of Iron-tellurides or BSCCO.

7 Acknowledgments

The author would like to greatly thank Dmitri K. Efetov, since this Master thesis is based on the assistance of one of his PhD projects. Without his technical support and the many helpful discussions it would not have been possible to master either the fabrication of these delicate devices nor the rather complex experiments. The same applies as well for the interpretation of the results. Furthermore, the author would like to thank the whole research group of Philip Kim and Prof. Philip Kim personally. This project was supported by Columbia University, New York City, in whose facilities the work was carried out. The exchange was supported by Prof. Christian Schönenberger (University of Basel) and the Swiss Nanoscience Institute (SNI).

References

[1] D. J. Quinn III and W. B. Ittner III, J. Appl. Phys. **33**, 748 (1962).

[2] H. Kamerlingh Onnes, Commun. Phys. Lab. Univ. Leiden **120b, 122b, 124b** (1911).

[3] W. Meissner and R. Ochesenfeld, Natureissenschaften **21**, 787 (1933).

[4] L. N. Cooper, Phys. Rev. **104**, 1189 (1956).

[5] J. Bardeen, L. N. Cooper, and J. R. Schrieffer, Phys. Rev. **106**, 162 (1957).

[6] J. Bednorz and K. Müller, Z. Phys. B **64**, 189 (1986).

[7] K. v. Klitzing, G. Dorda, and M. Pepper, Phys. Rev. Lett. **45**, 494 (1980).

[8] R. E. Peierls, Ann. I. H. Poincare **5**, 177 (1935).

[9] L. D. Landau, Phys. Z. Sowjetunion **11**, 26 (1937).

[10] K. S. Novoselov *et al.*, Science **306**, 666 (2004).

[11] K. Bolotin *et al.*, Solid State Communications **146**, 351 (2008).

[12] N. Levy *et al.*, Science **329**, 544 (2010).

[13] A. Deshpande, W. Bao, F. Miao, C. N. Lau, and B. J. LeRoy, Phys. Rev. B **79**, 205411 (2009).

[14] C. Dean *et al.*, Solid State Communications **152**, 1275 (2012).

[15] R. Decker *et al.*, Nano Lett. **11**, 2291 (2011).

[16] J. Xue *et al.*, Nat Mater **10**, 282 (2011).

[17] C. R. Dean *et al.*, Nat Nano **5**, 722 (2010).

[18] C. Weeks, G. Rosenberg, B. Seradjeh, and M. Franz, Nat Phys **3**, 796 (2007).

[19] D. A. Abanin, S. A. Parameswaran, S. A. Kivelson, and S. L. Sondhi, Phys. Rev. B **82**, 035428 (2010).

[20] D. J. Clarke, J. Alicea, and K. Shtengel, Nat Commun **4**, 1348 (2013).

[21] N. Lindner, Fractionalizing majorana fermions: non-abelian statistics on the edges of abelian quantum hall states.

[22] A. S. Mayorov *et al.*, Nano Lett. **11**, 2396 (2011).

[23] K. S. Novoselov *et al.*, Nat Phys **2**, 177 (2006).

[24] M. Orlita, W. Escoffier, P. Plochocka, B. Raquet, and U. Zeitler, Comptes Rendus Physique **14**, 78 (2013).

[25] S. Das Sarma, S. Adam, E. H. Hwang, and E. Rossi, Rev. Mod. Phys. **83**, 407 (2011).

[26] H. B. Heersche, P. Jarillo-Herrero, J. B. Oostinga, L. M. K. Vandersypen, and A. F. Morpurgo, Nature **446**, 56 (2007).

[27] Z. Jiang, Y. Zhang, Y.-W. Tan, H. Stormer, and P. Kim, Solid State Communications **143**, 14 (2007).

[28] M. Büttiker, Phys. Rev. B **38**, 9375 (1988).

[29] B. Jeckelmann and B. Jeannert, Rep. Prog. Phys. **64**, 1603 (2001).

[30] H. Ibach and H. Lüth, *Festkörperphysik - Einführung in die Grundlagen* (Springer, 2008).

[31] L. Shubnikov and W. de Haas, Proceedings of the Royal Netherlands Academy of Arts and Science **33**, 130 (1930).

[32] A. F. Andreev, Sov. Phys. JETP **19**, 1228 (1964).

[33] C. W. J. Beenakker, Rev. Mod. Phys. **80**, 1337 (2008).

[34] Aalto University, School of Science and Technology Report No., , 2010 (unpublished).

[35] C. W. J. Beenakker, Phys. Rev. Lett. **97**, 067007 (2006).

[36] R. Holm and W. Meissner, Z. Physik **74**, 715 (1932).

[37] W. Buckel and R. Kleiner, *Superconductivity: Fundamentals and Applications* (WILEY-VCH, 2004).

[38] S. Law Toner, *Magnetotransport in superconductor to semiconductor junctions: multiple Andreev reflections and coupling to quantum hall states*, PhD thesis, University of Illinois at Urbana-Champaign, 2012.

[39] T. Heikkilä, *Superconducting Proximity effect in mesoscopic metals*, PhD thesis, Helsinki University of Technology, 2002.

[40] G. E. Blonder, M. Tinkham, and T. M. Klapwijk, Phys. Rev. B **25**, 4515 (1982).

[41] N. Bogoliubov, J. Phys. (USSR) **11**, 23 (1947).

[42] G. E. Blonder and M. Tinkham, Phys. Rev. B **27**, 112 (1983).

[43] N. Alem *et al.*, Phys. Rev. B **80**, 155425 (2009).

[44] E. Jomehzadeh, A. Saidi, and N. Pugno, Physica E: Low-dimensional Systems and Nanostructures **44**, 1973 (2012).

[45] I. Naik and A. Rastogi, Pramana **76**, 957 (2011).

[46] T. Taniguchi and K. Watanabe, Journal of Crystal Growth **303**, 525 (2007).

[47] S. V. Borisenko *et al.*, Phys. Rev. Lett. **102**, 166402 (2009).

[48] G. D'Anna *et al.*, Phys. Rev. B **54**, 6583 (1996).

[49] D. Dew-Hughes, Low Temperature Physics **27**, 713 (2001).

[50] H. Courtois, P. Charlat, P. Gandit, D. Mailly, and B. Pannetier, Journal of Low Temperature Physics **116**, 187 (1999).

[51] X. Jehl, M. Sanquer, R. Calemczuk, and D. Mailly, Nature **405**, 50 (2000).

[52] G. Sheet, S. Mukhopadhyay, and P. Raychaudhuri, Phys. Rev. B **69**, 134507 (2004).

[53] X. Lu, *Point-contact Andreev reflection studies on superconductors*, PhD thesis, University of Illionois, 2010.

[54] D. Daghero and R. S. Gonnelli, Superconductor Science and Technology **23**, 043001 (2010).

[55] K. Komatsu, C. Li, S. Autier-Laurent, H. Bouchiat, and S. Gueron, Superconducting proximity effect through graphene from zero field to the quantum hall regime, arXiv:1202.1690.

[56] L. Shan *et al.*, Phys. Rev. B **68**, 144510 (2003).

[57] Y. G. Naidyuk and I. K. Yanson, *Point Contact Spectroscopy* (Springer, 2005).

[58] M. Tinkham, *Introduction to superconductivity* (Dover, 1996).

[59] S. Bhattacharya and M. Higgins, Phys. Rev. B **49**, 1005 (1994).

[60] U. Yaron *et al.*, Phys. Rev. Lett. **73**, 2748 (1994).

[61] S. Ramakrishnan *et al.*, Physica C: Superconductivity **256**, 119 (1996).

[62] J. Schiefele, F. Sols, and F. Guinea, Phys. Rev. B **85**, 195420 (2012).

[63] T. Taychatanapat, K. Watanabe, T. Taniguchi, and Jari, Nature Physics , in press (2013).

Supporting material

Control experiments with MLG-$NbSe_2$-MLG devices

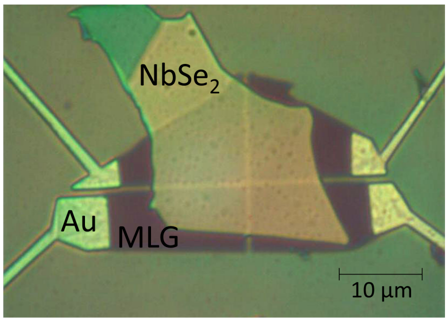

(a)

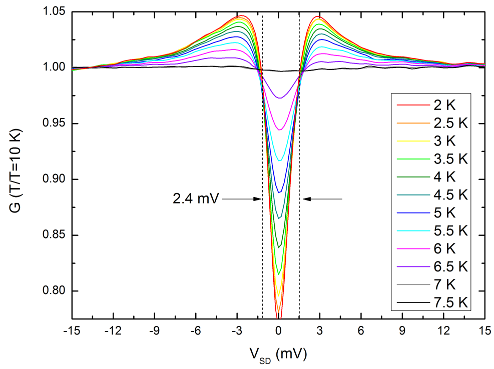

(b)

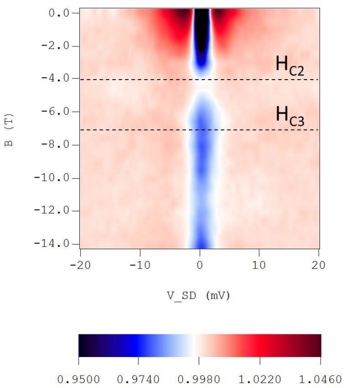

(c)

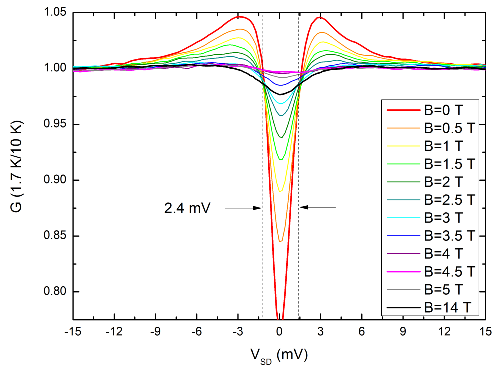

(d)

Figure 17: **a)** Optical image of the control device. **b)** 2-terminal differential conductance across the SN junction of a MLG-$NbSe_2$-MLG control device for different temperatures. **c)** Normalized differential conductance ($1\ K/\ 10\ K$) for different magnetic fields. **d)** Line cuts for different magnetic fields.

The properties of the SN interface between $NbSe_2$ and graphene/graphite was investigated with devices of the structure MLG-$NbSe_2$-MLG, as shown in fig. 17a.

In fig. 17b the temperature dependence of the normalized differential conductance across the SN junction is shown. The maximal signal-to-background ratio of the differential conductance was found to be in the order of 5% at 2 K.

The magnetic field dependent behavior of the normalized differential conductance is shown in fig. 17c and fig. 17d (line traces). The zero bias dip at $V_{SD}= 0\ mV$ and the enhanced differential conductance disappear at $\sim$4 T, which is in good agreement with H_{C2} at 1.7 K. By further increasing the magnetic field, a small dip at $V_{SD}= 0\ mV$ remained until 14 T. This zero bias anomaly is a common feature observed for PCARS. Whether surface conductivity, which exists up to $H_{C3} \sim 6.7\ T$ at 1.7 K [48], is visible in these samples is hard to judge since the ever present zero bias anomaly makes it difficult to pin-point the field at which the superconducting state vanishes.